Modeling and Trajectory Control of a Transitioning Quadrotor Biplane Tailsitter

Jean-Paul Reddinger
Aerospace Engineer
U.S. Army Combat Capabilities Development Command
Army Research Laboratory
Aberdeen Proving Ground, MD, USA

Kristoff McIntosh
Graduate Student

Di Zhao
Graduate Student

Sandipan Mishra
Professor

Center for Mobility with Vertical Lift
Rensselaer Polytechnic Institute
Troy, NY, USA

ABSTRACT

A comparison study between modeling approaches of a quadrotor biplane tailsitter aircraft is conducted. A blade element theory model with dynamic inflow is used to validate a reduced order model that incorperates a simple interference model for trajectory planning and dynamic simulation. With an appropriate interference model, the predicted power requirement through transition from hover to forward flight drops by 30-45% as the interference velocity reduces the effective angle of attack for the wing. A trajectory generation scheme is developed, which shows the importance of accurate stall modeling for the transition maneuver. Without interference modeling all transition trajectories are expected to violate the installed motor power limit or pass through an excessively stalled wing state ($> 60^\circ$). The interference model dynamics are used to design a trajectory that avoids stall of the aircraft by adding a vertical climb element to the transition maneuver. A transition controller is linear dynamic inversion transition controller is described for inner loop stability over the entire flight regime.

NOTATION

$\mathbf{A}$	linearized system matrix
$\mathbf{B}$	linearized input matrix
C_T	thrust coefficient ($T/\rho\pi\Omega^2R^4$)
C_Q	torque coefficient ($Q/\rho\pi\Omega^2R^5$)
J	advance ratio in the axial direction ($V/\Omega R$)
P	power requirement (hp)
Q	rotor torque (ft-lb)
R	rotor radius (ft)
T	rotor thrust (lb)
$\mathbf{u}$	vehicle control vector
V	free stream velocity
V_{disk}	inflow velocity
V_{wake}	wake velocity
$\mathbf{x}$	vehicle state vector
$\mathbf{y}$	vehicle controlled output vector
α	angle of attack (deg)
α_e	wing effective angle of attack including interference (deg)
β	sideslip angle (deg)
γ	flight path angle of wind frame relative to world frame (deg)
χ	flight azimuth of wind frame relative to world frame (deg)
η	decay ratio of rotor wake velocity at wing
ϕ	vehicle pitch attitude (deg)
ρ	air density (slug/ft^3)
σ	bank angle of wind frame relative to world frame (deg)
Ω_0	collective rotor speed (rad/s)
Ω_P	differential pitch rotor speed (rad/s)
Ω_R	differential roll rotor speed (rad/s)
Ω_Y	differential yaw rotor speed (rad/s)

Presented at the Vertical Flight Society 75th Annual Forum & Technology Display, Philadelphia, Pennsylvania, May 13–16, 2019.

INTRODUCTION

The U.S. Army has identified unmanned aerial systems (UAS) as having an important role in the future of Army aviation (Ref. 1). A diverse set of new and improved capabilities are expected to be introduced by autonomous UAS platforms, which are being targeted as part of the Future Vertical Lift (FVL) component of the U.S. Army's modernization priorities (Ref. 2). Future UAS applications may include aerial resupply; intelligence, surveillance, and reconnaissance; elec-

tronic attack; and advanced teaming between manned and unmanned systems. Reference 1 defines a categorization of UAS sizes that can be used to differentiate vehicle weights and flight capabilities. Table 1 summarizes the capability sets for each of these groups. Vertical take-off and landing (VTOL) aircraft have typically been absent from the group 2-4 design space due to poor power-weight ratios at small scales for gas-powered configurations, and insufficient energy density for battery-powered configurations. More recently, advances in electric propulsion, electronics, manufacturing and material technologies has opened this design space for novel VTOL aircraft configurations.

Table 1. U.S. Army UAS Groups.

Group	GTOW (lb)	Altitude (ft)	Speed (kt)
1	<20	<1,200 AGL	<100
2	21-55	<3,500 AGL	<250
3	<1,320	<18,000 MSL	<250
4	>1,320	<18,000 MSL	Any
5	>1,320	>18,000 MSL	Any

The University of Maryland has been actively researching a quadrotor biplane tailsitter UAS configuration. They have manufactured scaled designs under 1 lb (Ref. 3), as well as in the 6-8 lb range (Refs. 4–6). These aircraft have demonstrated interesting control problems, including a lack of roll authority in forward flight (which was solved by canting the rotors in Reference 4), as well as the availability of control redundancy with the inclusion of both RPM control and blade pitch control (Ref. 5). Industry partners like Bell have also been pursuing development of this configuration, with the Autonomous Pod Transport (APT) intended to scale from payload capacities of 70 lb to 1,000 lb (Ref. 7). In a cooperative research effort between the U.S. Army Combat Capabilities Development Command Army Research Laboratory (ARL) and University of Maryland, a 20 lb gross weight version of the quadrotor biplane tailsitter platform, called the Common Research Configuration (CRC-20) (Ref. 8). This vehicle (pictured in Figure 1) represents the upper end of the group 1 weight class.

Fig. 1. Photograph of the CRC-20 aircraft

Table 2. Specifications of the CRC-20 prototype

Specification	Measurement
Gross Weight	21.0 lb
Rotor Diameter	2.0 ft
Rotor Type	XOAR 24×10
Wing Span	4.9 ft
Power Plant	Li-Ion Battery

Inherent to the CRC-20 platform is the need for a transition from hover to forward flight, and forward flight back to hover over the duration of a mission. This transition has the potential to pass through wing-stall which produces highly non-linear behavior and may present a significant challenge for robust control of the vehicle (Refs. 9, 10). The vehicle dynamics through low speed transition are dominated by interference between the rotor and the wing (Ref. 11), and sufficient modeling capabilities are necessary to design and test a trajectory that smoothly transitions, especially as the vehicle scales up and thrust-to-weight ratios diminish.

In Reference 9, the rotor and wing are modeled as isolated aerodynamic bodies, neglcting interference. The resulting model predicts a power requirement at moderate speeds between hover and the wing stall speed that was 5% higher than the hover power. In Reference 12, flight tests of an 8 lb quadrotor biplane exhibited a monotonic reduction in power requirement with increasing flight speed which suggested that wing stall was less prominant than the model in Reference 9 was predicting.

In an effort to improve the accuracy of the analysis, this study will explore the effects of interference modeling on the dynamics of the CRC-20. The improved model will be used to produce a trajectory generation and control framework that can operate over the range of orientations the aircraft will encounter throughout its flight envelope.

MODELING AND ANALYSIS

The CRC-20 configuration uses four independent rotors for thrust in hover, and operates similarly to a standard quadrotor with fixed pitch rotors. The vehicle controls are defined as a set of orthogonal control modes, relative to the hovering orientation of the body. In hover, increasing the collective control increases the rotor speed of all four rotors. Increasing differential roll increases the speed of the left rotors and reduces the speed of the right rotors, causing a roll-right moment on the hovering aircraft. Increasing differential pitch increases the speed of the rear rotors while reducing the speed of the front rotors to put a nose-down moment on the aircraft. Increasing differential yaw increases the rotor speed of the front-right and rear-left rotors, while reducing the rotor speed of the rear-right and front-left rotors which induces a nose-right moment on the aircraft.

The aircraft transitions to a forward flight orientation by pitching 90 degrees nose down. In forward flight mode a set of parallel wings produce lift and the rotors produce thrust to overcome drag. The previously defined control definitions for

rotor speed do not change, but rotate with the body. Relative to the forward flight body orientation in the inertial frame, differential roll affects aircraft heading, and differential yaw affects aircraft bank angle.

For simulation and analysis of conventional rotorcraft configurations, the standard Z-Y-X Euler convention is satisfactory. The traditional vehicle definition is shown in Figure 2. In this convention, however, gimbal lock will become an issue at pitch attitudes of $\pm 90^\circ$. For a tail-sitter aircraft such as the CRC-20, it is expected that the aircraft will pass through 90° of pitch attitude as it converts from hover to forward flight mode and vice versa.

In order to be able to simulate the full flight profile of such an aircraft, the traditional Euler convention cannot be used. Instead, the vehicle is defined such that the nose is positive-y in the inertial frame and the left wing is in the positive-x direction, as shown in Figure 3. In this convention ϕ represents the vehicle pitch attitude (positive nose-down) and θ represents the vehicle roll attitude (positive right wing-down). The ψ heading definition remains unchanged, but the analysis is initialized with a -90° heading to position the aircraft with the appropriate orientation relative to the free stream velocity in forward flight.

Blade Element Threory Model

A blade element theory model is constructed in FLIGHTLAB to perform trim sweeps of the aircraft. The FLIGHTLAB model uses a blade element theory model to solve for rotor forces and moments, with a 1×1 dynamic wake model for the inflow of each rotor. The 10° lateral cant angle of the rotors used in (Ref. 4) to increase the roll authority of the vehicle in forward flight mode is preserved.

Total blade mass properties are found from total mass data on the XOAR PJP propellers, with sectional mass assumed to be constant along the span. In the absence of propeller performance data for the rotors, the blade sectional aerodynamic properties use the 74.8% span characteristics of the SUI rotor as a representative airfoil section (Ref. 13).

The wings are modeled as aerodynamic surfaces with quasi-steady airfoil properties for a Wortmann FX63-137 airfoil. All structural elements are assumed to be completely rigid, and two spanwise aerodynamic control points are used for each wing. The built in incidence angle between the chord line of the wing and the fuselage chord line is zero. The fuselage drag uses a constant 0.0151 coefficient of drag, with no lift, side force, or aerodynamic moments modeled.

Aerodynamic interference from the rotor to the wing is modeled using finite state interference, which propogates each state of the dynamic inflow from the rotor plane to a maximum distance of six rotor radii. The total interference velocity is then added to the freestream velocity at each wing aerodynamic control point to produce an effective angle of attack for that wing segment, which differs from the angle of attack relative to the freestream velocity. No upwind intereference effect is modeled from the wings onto the rotors.

Reduced Order Flight Dynamics Model

Using the FLIGHTLAB blade element theory model, a range of forward flight speeds and vertical flight speeds are used to produce a two dimensional trim sweep. For each unique flight condition, rotor thrust and torque are recorded along with rotor speed and total freestream velocity at the rotor hub. This data is used to construct a quadratic regression model of rotor thrust and torque coefficient as a function of the advance ratio relative to the axial component of the freestream (J). The resulting two reduced order rotor models are shown in Figure 4, along with the data that was used to produce them. Both models have an R^2 value in excess of 0.98, indicating good fit over the expected flight envelope.

In order to calculate the effect of the rotor interference on the wing, a simplified interference model is derived from momentum theory. The inflow at the rotor disk can be solved from momentum theory using the following equation.

$$V_{disk} = \sqrt{\frac{T}{2\rho\pi R^2}} \tag{1}$$

According to momentum theory, the wake velocity after contraction is equal to twice the inflow velocity at the disk, however an empirical term η is added to account for wake velocity decay through viscosity and other effects.

$$V_{wake} = 2\eta V_{disk} \tag{2}$$

When solving for the aerodynamic force of each wing segment, this velocity is added to the freestream velocity to produce a change in the total wing dynamic pressure and effective angle of attack.

Figure 5 shows a set of trim sweeps done for the CRC-20, with several different modeling approaches—The dynamic inflow FLIGHTLAB model with no interference, the FLIGHTLAB model with interference, the reduced order model with no interference, and the reduced order model with interference at several values of η. The figure plots the rear/top wing's effective angle of attack as a function of the trimmed flight speed and the FX63-137 stall angle of 12.9° is marked with as a dashed line.

This figure shows good general agreement between the dynamic inflow model and the reduced order model derived from it. The two modeling approaches without interference predict wing angle of attacks that are within 5° in the stalled state, and within 1° of each other at cruise speeds greater than 22 kt. These models show the discontinuity between hover mode and forward flight mode that exists without interference. The trimmed wing angle of attack over 30° up to 20 kt, while beyond 22 kt the wing trims at less than 10° angle of attack. Figure 6 shows the effect this trim discontinuity has on the power curve, with an even larger disconituity when the flow over the wing reattaches beyond the stall speed.

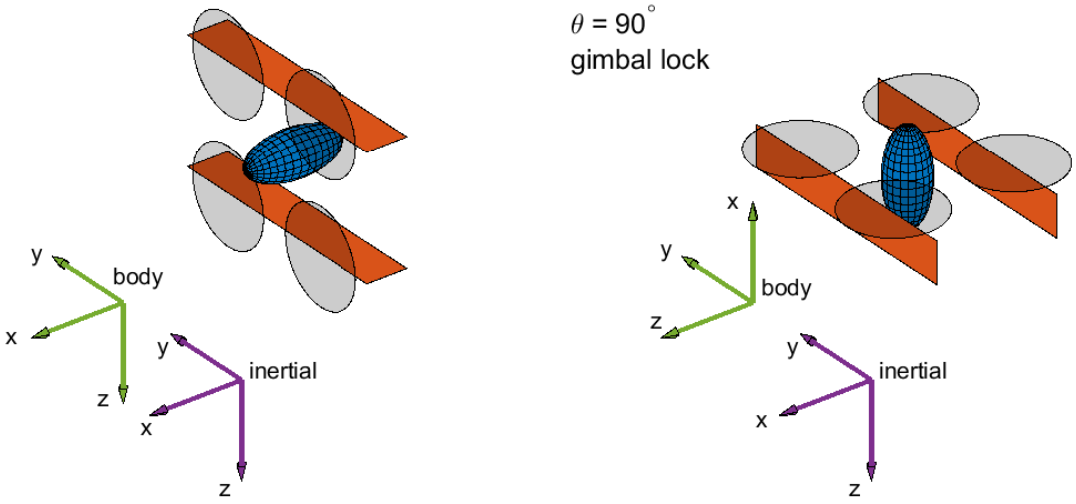

Fig. 2. Z-Y-X Euler convention.

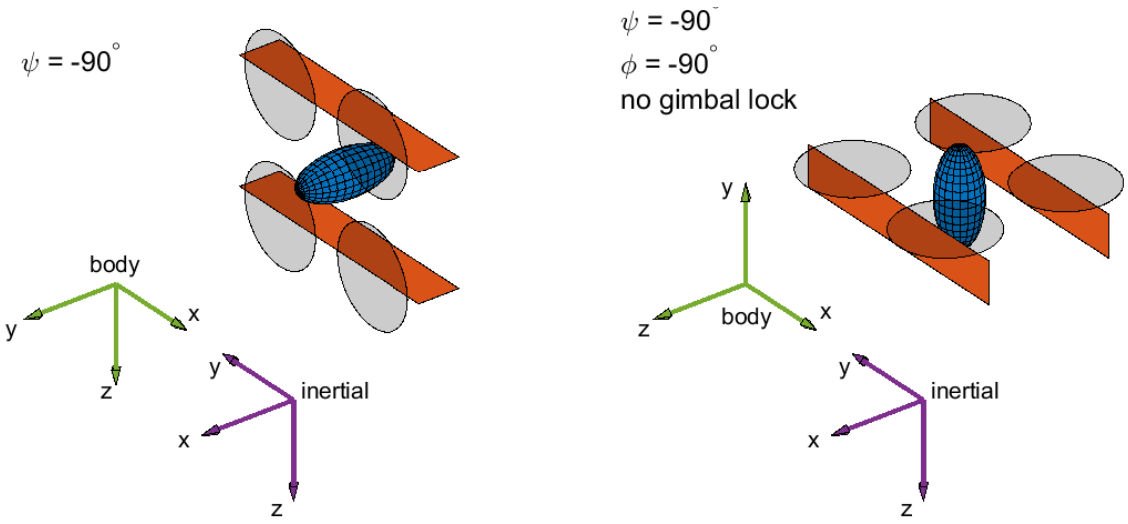

Fig. 3. Z-X-Y Euler convention.

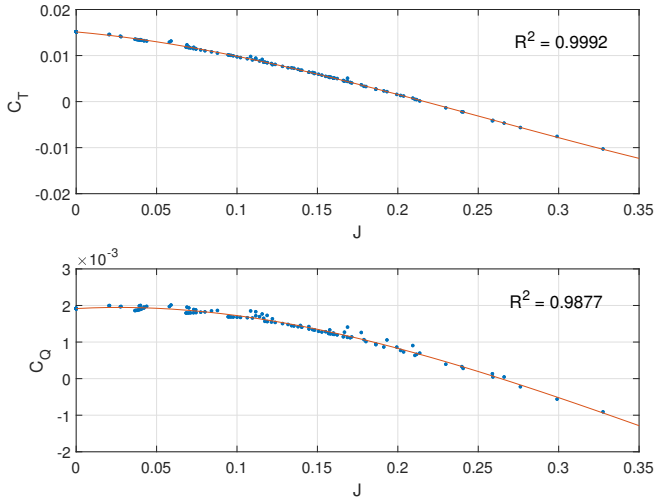

Fig. 4. Rotor thrust and torque coefficients parameterized by advance ratio

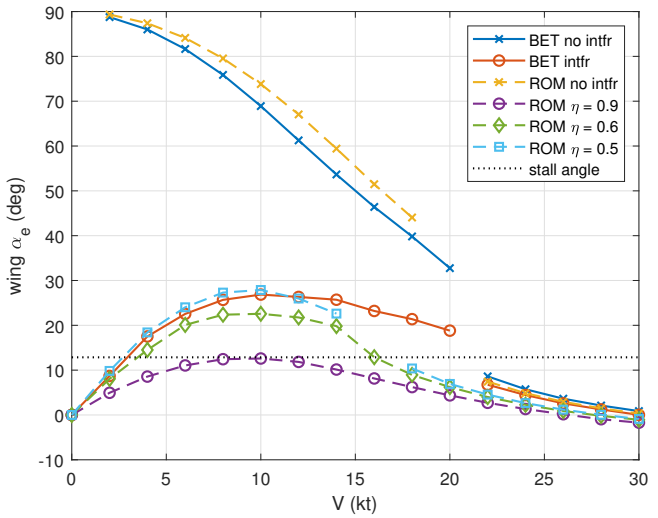

Fig. 5. Wing angle of attack (deg) versus velocity (kt) for various modeling approaches

Figures 5 and 6 also include results using both interference models. For all interference models, hover and near-hover flight speeds show the effective wing angle attack being much lower, with at least 3 kt forward velocity required for the wing to stall. At about 4 kt, the wing effective angle of attack stalls for the finite state interference model, and the angle maxes out at about 10 kt, never exceeding 30°. The corresponding power curve shows a reduction in power requirement for all flight speeds with the reduced wing angle of attack.

Furthermore, the figures demonstrate that η selection has a significant influence on the vehicle stall prediction through transition. For an η of 0.9, 90% of the inflow velocity is preserved in the wake. For the entire range of flight speeds shown in Figure 5, the wing angle of attack remains below the 12.9° stall angle.

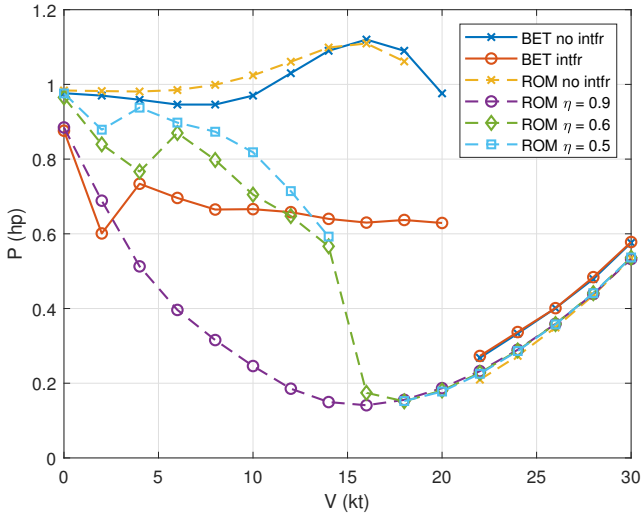

Fig. 6. Total power requirement (hp) versus velocity (kt) for various modeling approaches

An interference model with an η of 0.5 to 0.6 produces a more similar behavior to the finite state interference model for speeds up to about 15 kt. At speeds above 15 kt, the reduced order interference models overpredict the interference velocity added to the wing, which causes a reduction in the wing stall speed from about 22 kt to 16-18 kt.

During transition, η selection has an even more significant effect on the power prediction. On Figure 6, the interference model can change the power requirement by up to 80% during transition, and depends greatly on the stall state of the wing. This behavior indicates the importance of interference modeling on both stall prediction and power prediction, as well as the extent of uncertainty that may result from entering stall.

Constraints to Transition Trajectory

During the transition maneuver of the CRC-20, this section will consider two constraints that have the potential to impact trajectory planning: the wing stall angle, and the maximum power availabile at the motors. Figures 7 and 8 plot the power requirement predictions for the reduced order model with no interference, and for the reduced order model with interference respectively. For these results, η is chosen to be 0.6, as that value gave the closest agreement to the finite state interference model in Figures 5 and 6. This data is generated from a two dimensional trim sweep through velocity magnitude (from 0 kt to 35 kt in increments of 5 kt) and flight path angle (from -30° to 90° in increments of 15°).

In Figures 7 and 8, contours of trimmed power requirement are plotted against velocity magnitude on the x-axis and flight path angle on the y-axis. The maximum available power limit of 1.1 hp is marked, to show the upper limit on feasible trim states that exist on this figure. The major difference between these figures is visible at flight path angles less than 60° and speeds less than 25 kt. For the model with no interference, this

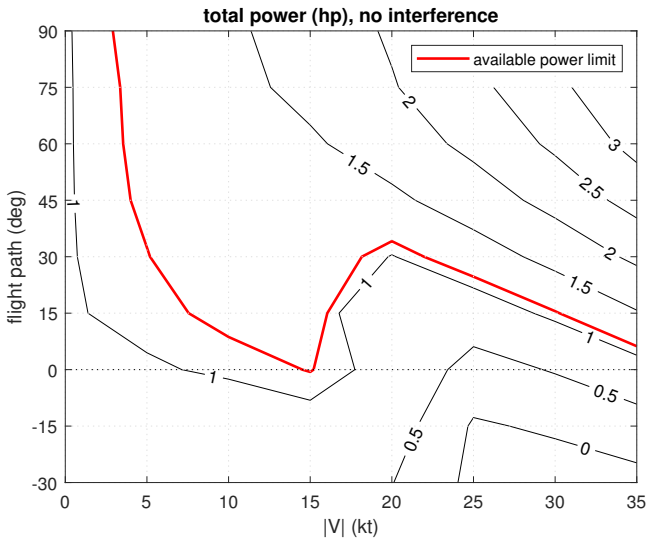

Fig. 7. Total power requirement (hp) as a function of speed (kt) and flight path angle (deg) with no interference modeling

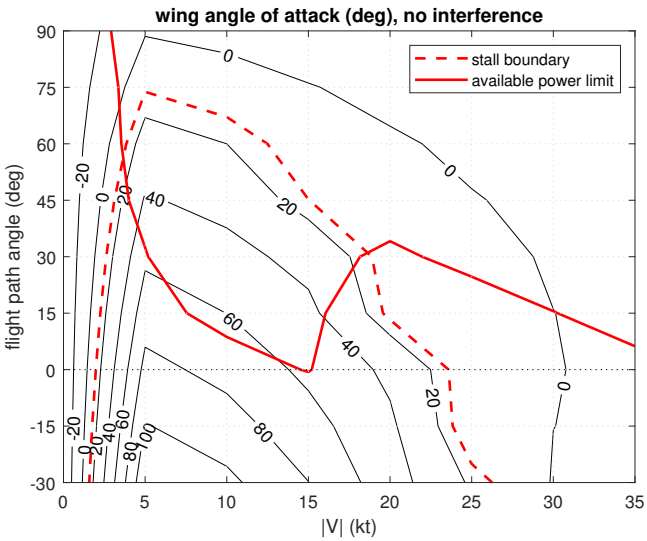

Fig. 9. Wing angle of attack (deg) as a function of speed (kt) and flight path angle (deg) with no interference modeling

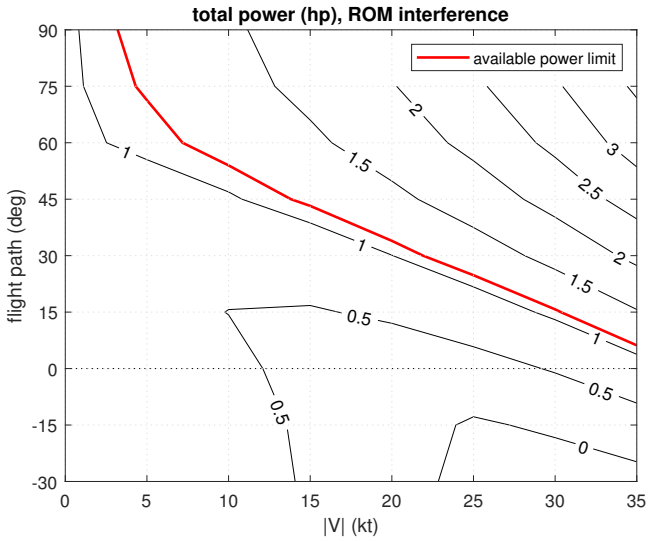

Fig. 8. Total power requirement (hp) as a function of speed (kt) and flight path angle (deg) with reduced order interference modeling

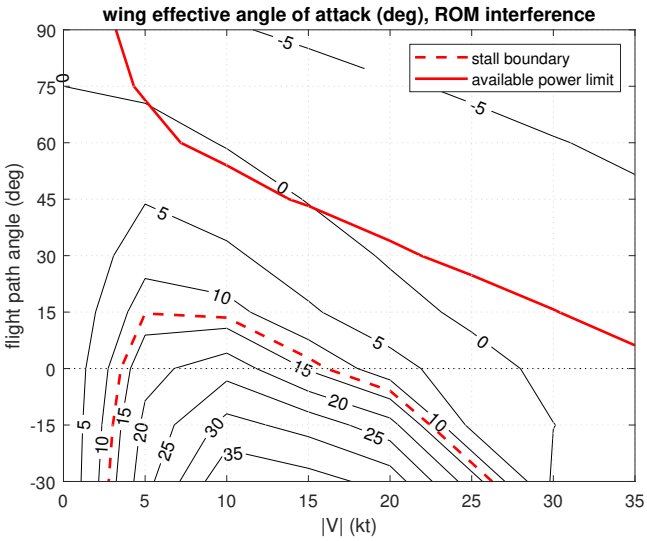

Fig. 10. Wing effective angle of attack (deg) as a function of speed (kt) and flight path angle (deg) with reduced order interference modeling

is where the added drag of wing stall significantly impacts the power requirement, described in detail in Reference 9.

The effect of interference velocity is to bias the angle of attack of the wing at all flight conditions towards the built-in incidence angle of the wing, while increasing the dynamic pressure. This effect was shown in Figure 5, where increases in the η interference velocity term resulted in a reduction in the effective angle of attack of the wing throughout the envelope. A trajectory that includes a stalled wing segment can be expected to encounter more complex flight dynamics, with behavior that may include control reversal, highly nonlinear aerodynamics, and higher power requirements. It is gerenarlly desirable to avoid these conditions if possible.

Comparing Figures 9 and 10 shows that the stall angle of the wing—marked with the dashed line—is present across the range of trim states examined. The higher angles of attack and power requirements predicted by the model with no interference in Figure 9 predict that it is impossible to design a trajectory that does not violate the stall or power limit boundary condition.

Figure 10—the model with interference—has a larger set of feasible flight conditions due to a reduction in both the power requirement and wing angle of attack. While the stall boundary of the wing has receeded relative to Figure 9, level flight and descending flight will both still cross the stall boundary at speeds above 3 kt. A trajectory that includes a small ascent

velocity, such that the flight path angle exceeds 15° would be able to avoid stall completely according to this model. For a less optimistic estimation of the stall boundary, however, such as the one given by the finite state interference model pictured in Figure 11, the flight path angle must exceed 25° to avoid stall at 10 kt.

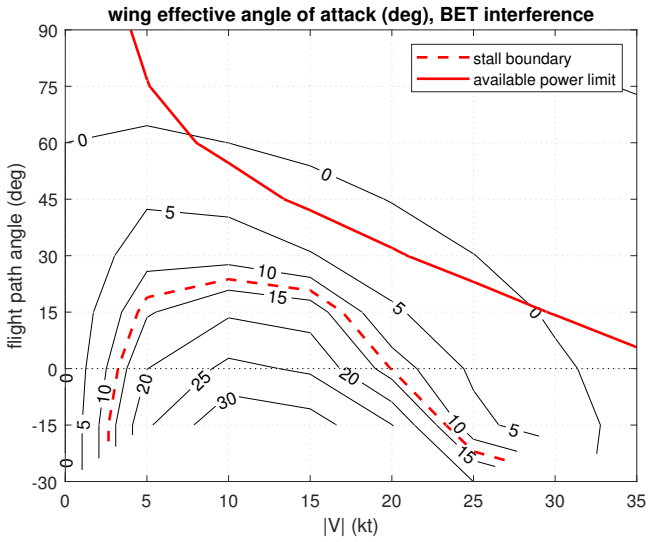

Fig. 11. Wing effective angle of attack (deg) as a function of speed (kt) and flight path angle (deg) with BET interference modeling

To design a trajectory for transitions between hover and forward flight, reliably avoid stall, and prevent motor power saturation, these figures demonstrate the importance of accurate interference modeling between the wing and the rotor.

TRAJECTORY PLANNING AND CONTROL

Coordinate Systems for Modeling, Guidance and Control

Though the modeling of the dynamics is performed in the traditional world/body frame, a wind-frame coordinate system is used for trajectory planning. The schematic showing the relationship between world frame, wind frame and body frame is shown in Figure 12. In the wind-frame, V is the airspeed; γ is the flight path angle; χ is the flight azimuth; α is the angle of attack; β is the sideslip angle; and σ is the bank angle. Note that these angles can be calculated by projecting the velocity vector $\mathbf{V}$ onto the $X-Y$, $X-Z$ and $Y-Z$ inertial (or body) frames respectively, as shown in Figure 12. The relationship between these angles is captured by the rotational equivalence

$$T_1(\sigma)T_2(\gamma)T_3(\chi) = T_3(\beta)T_2(-\alpha)T_1(\phi)T_2(\theta)T_3(\psi) \quad (3)$$

It is worth noting that for feedback control, IMU measurements are obtained in the body frame, while GPS measurements are collected in the inertial frame.

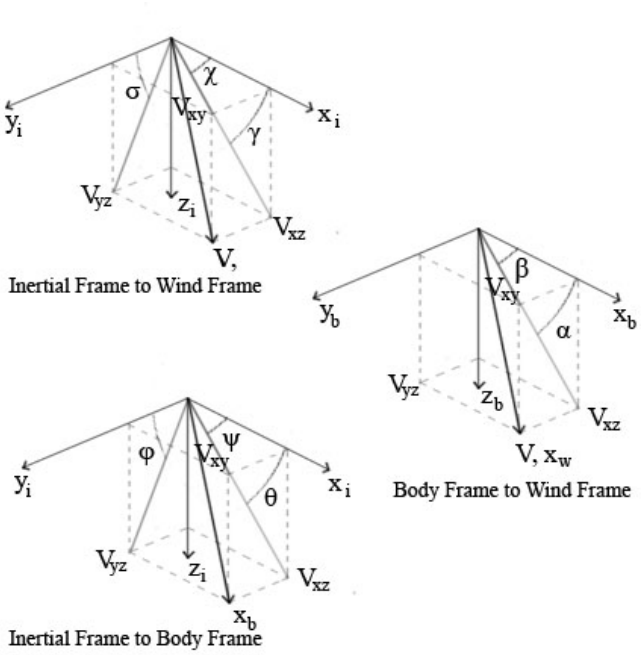

Fig. 12. Illustration of the Inertial, Body, and Wind Frames.

Overall Control Architecture

The overall control architecture shown in Figure 13 is proposed to fulfill the flight mission. In this architecture, the outer-loop path planner and the inner-loop attitude/airspeed controller are organized in a cascaded structure to control the CRC-20.

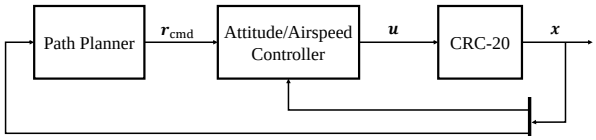

Fig. 13. Overall control architecture.

Based on the mission objective and the current state of the plant, represented by:

$$\mathbf{x} = [x, y, z, \phi, \theta, \psi, u, v, w, p, q, r]^T \quad (4)$$

the path planner designs the reference trajectory *in the wind-frame* that guides the vehicle from its current flight state to the desired flight state. Note that the path planning can also be accomplished in a purely feedforward fashion, instead of being designed on-the fly. For the rest of this paper, we consider the case where the commands for the reference trajectory are computed *ahead of time*, and are represented by:

$$\mathbf{r}_{\text{cmd}} = [V_{\text{cmd}}, \gamma_{\text{cmd}}, \chi_{\text{cmd}}, T_{\text{cmd}}, \alpha_{\text{cmd}}, \beta_{\text{cmd}}, \sigma_{\text{cmd}}]^T \quad (5)$$

where V denotes the airspeed; γ denotes the flight path angle; χ denotes the flight azimuth; T denotes thrust; α denotes the

angle of attack; β denotes the sideslip angle; and σ denotes the bank angle. These commands are then fed into the attitude/airspeed controller. This controller then tracks the above commands by a feedback mechanism (described in a subsequent section). This inner loop controller generates corrections to the collective RPM (Ω_0), the differential roll RPM (Ω_R), pitch RPM (Ω_P) and yaw RPM (Ω_Y), respectively. The resultant RPM inputs are then mapped into commands for RPMs of individual rotors.

$$\mathbf{u} = [\Omega_1 \;\; \Omega_2 \;\; \Omega_3 \;\; \Omega_4]^T. \tag{6}$$

The Path Planner

The structure of the outer-loop path planner is shown in Figure 14. The core of the path planner determines the trajectory

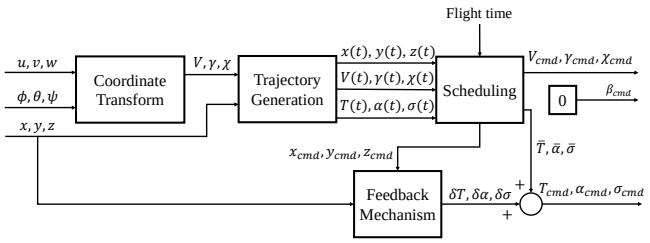

Fig. 14. Outer-loop path planner structure.

based on a simplified 3 degree of freedom (DOF) model of the vehicle. This model regards the vehicle as a point mass. The position of the vehicle is determined by (x,y,z) in the north-east-down (NED) frame; the magnitude and orientation of the vehicle's velocity is determined by (V,γ,χ); the thrust and lift exerted on the vehicle are determined by (T,α,σ), which are virtual inputs and assumed to have instantaneous response. After the generation of the trajectories of the above variables as parametric functions of time t, the real-time commands can be scheduled based on the current flight time. Here, an outer-loop feedback mechanism is used to compensate for the errors between the actual position (x,y,z) and position commands $(x_{cmd}, y_{cmd}, z_{cmd})$. On the other hand, the execution of the velocity-related commands $(V_{cmd}, \gamma_{cmd}, \chi_{cmd})$ and force-related commands $(T_{cmd}, \alpha_{cmd}, \sigma_{cmd})$ are fulfilled by the inner-loop controller. In the following development, the subscript *cmd* is dropped for brevity.

Trajectory Generation Approach

A simplified scenario will be described to illustrate trajectory generation, with the following assumptions:

(1) The flight path is divided into three different segments, each of which represents different flight modes: hover/ascent, the transition, and forward flight.

(2) The transition phase is initiated after reaching a *known* critical velocity V_c. The transition is complete with a known forward flight velocity V_{FF}. The transition path is assumed to be purely in the $X-Z$ inertial frame.

(3) The entire trajectory is only planned once and implemented in a feedforward manner. No iterative replanning is performed.

Ascent: The airspeed velocity trajectory in ascent, from zero to the critical velocity V_c, is designed to be constant acceleration along the down facing axis of the inertial frame of the CRC-20, as follows:

$$z(t) = \frac{1}{2}a(t-t_0)^2 + z_0, \;\; V(t) = a(t-t_0), \;\; T(t) = m(a+g) \tag{7}$$

where a is the specified (negative) acceleration of the CRC-20 during ascent and t_0 is the time of launch. Since the ascent is purely vertical, the desired flight path angle $\gamma_d(\cdot)$ trajectory is constant at $\pi/2$ radians. All the other output angle trajectories $(\alpha_d,\ \beta_d,\ \sigma_d,\ \chi_d) \equiv \mathbf{0}$ in the inertial frame. The end-time of the ascent phase is $t_1 = t_0 + \frac{V_c}{a}$, and the corresponding height achieved at this time, $z_1 = z(t_1)$.

Transition to forward flight: After launch, the CRC-20 enters the transition to forward flight. Though the flight path for transition may be parameterized in several ways, we assume an ellipse in the $X-Z$ plane, as shown in Figure 15, with the ascent and forward flight trajectories being tangent to the semi-major and semi-minor axes, respectively; described by

$$\begin{aligned} x(t) &= a\cos(\zeta(t)) + x_0 \\ z(t) &= b\sin(\zeta(t)) + z_1 \end{aligned} \tag{8}$$

It is important to note that $\zeta(\cdot)$ governs the speed of the transition and consequently the evolution of $V(\cdot)$ with respect to time along the ellipse. The choice of the profile $\zeta(\cdot)$, and the ellipse parameters a, and b together define a single transition trajectory and thus are the design variables.

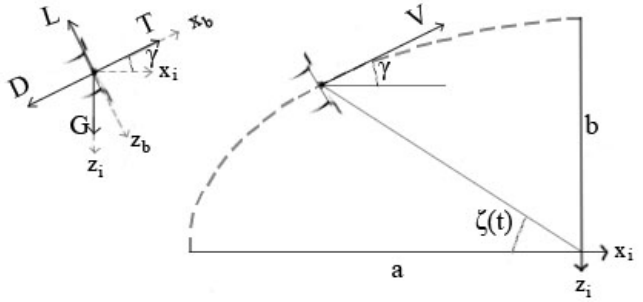

Fig. 15. Illustration of the elliptical flight path for transition. Left inset: simplified dynamics of a point mass on the elliptical curve. T denotes thrust, G is gravity, D is drag, and L is the lift force.

The flight path velocity and flight path angle can be calculated from $\zeta(\cdot)$, a, and b through

$$\begin{aligned} V(t) &= \sqrt{\dot{x}(t)^2 + \dot{z}(t)^2} \\ &= \dot{\zeta}(t)\sqrt{a^2\sin^2(\zeta(t)) + b^2\cos^2(\zeta(t))} \\ \gamma(t) &= \arctan\left[\tfrac{dz}{dx}\right] = \arctan\left[-\tfrac{b}{a}\cot(\zeta(t))\right] \end{aligned} \tag{9}$$

In order to determine the profile for thrust $T(t)$ and angle of attack $\alpha(t)$, we trim the aerodynamic forces (thrust T, lift L, drag D, and gravity $G = mg$) acting on aircraft along the elliptical trajectory, as illustrated in the inset in Figure 15. The two equations of motion at any time instant are given by:

$$\begin{aligned} T(t) - D(t) - G\sin(\gamma(t)) &= m\dot{V}(t) \\ L(t) - G\cos(\gamma(t)) &= \frac{mV(t)^2}{R(t)}. \end{aligned} \tag{10}$$

$R(t)$ is the radius of the curvature of the elipse:

$$R(t) = \frac{ab}{\left(a^2\sin^2(\zeta(t)) + b^2\cos^2(\zeta(t))\right)^{\frac{3}{2}}} \tag{11}$$

Given a profile $V(t)$, $\zeta(t)$, and a, b, we can use these equations to calculate $L(t)$ and $T(t)$.

Finally, the lift profile $L(t)$ is used to determine the profile for the angle of attack:

$$\alpha(t) = \frac{2L(t)}{C_{L\alpha}V(t)S} \tag{12}$$

where $C_{L\alpha}$ is the lift curve slope of the wings and S is the biplane wing area.

The trajectories for $\beta(t) = \sigma(t) = \chi(t) \equiv 0$ during the transition. This is a direct consquence of the fact that the transition occurs purely in the $X - Z$ plane.

Parameterization, Constraints and Feasibility: The profile $\zeta(\cdot)$ can be parameterized in a variety of ways. In the simplest scenario, a profile is chosen of the form $\dot{\zeta}(t) = \omega_0 + k(t - t_1)$, i.e., a constant angular acceleration profile that guarantees smoothness. a, b, ω_0, and k then become the design parameters for the trajectory. The final time for completion of the transition can be obtained by solving $\frac{\pi}{2} = \omega_0(t_2 - t_1) + \frac{1}{2}k(t_2 - t_1)^2$.

The designed trajectory must satisfy several constraints

$$V(t_1) = V_c \qquad V(t_2) = V_{FF} \tag{13}$$

$$T(t) \in [T_{min},\ T_{max}] \qquad \dot{V} \in [a_{min},\ a_{max}] \tag{14}$$

Furthermore, in order to guarantee flyability, the trajectories generated must be within the feasible flying region, discussed earlier with Figure 10.

Forward Flight: Once the vehicle completes the transition and enters forward flight at velocity V_{FF}, all output trajectories are held at constant values, with $V(t)$ and $\alpha(t)$ being the necessary trim values needed to maintain speed, and all other output angle trajectories (β, σ, γ, χ) being set to 0 radians.

According to the trajectory generation method discussed above, a reference trajectory consists of the ascending, transition and forward flight phase is shown in Figure 16.

Figure 18 shows the flight path angle versus airspeed space of the planned trajectory. The planned trajectory (drawn in blue) lies inside the corridor formed by the stall boundary and the power limit. Hence, when flown close to the quasi-equilibratory state, the trajectory will indeed be flyable.

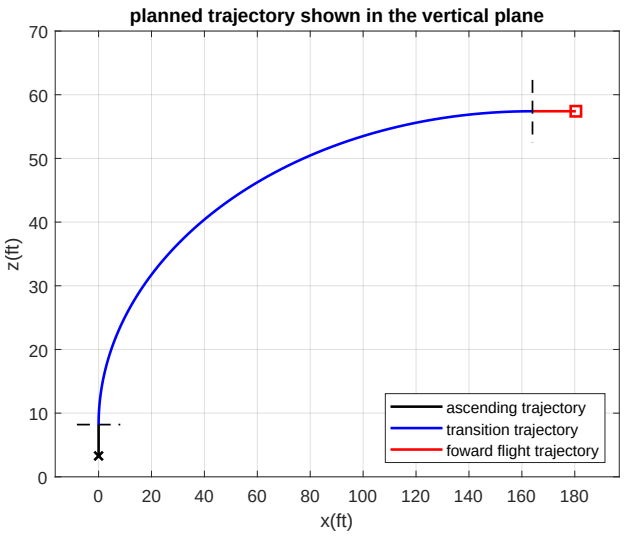

Fig. 16. Planned trajectory shown in the vertical plane

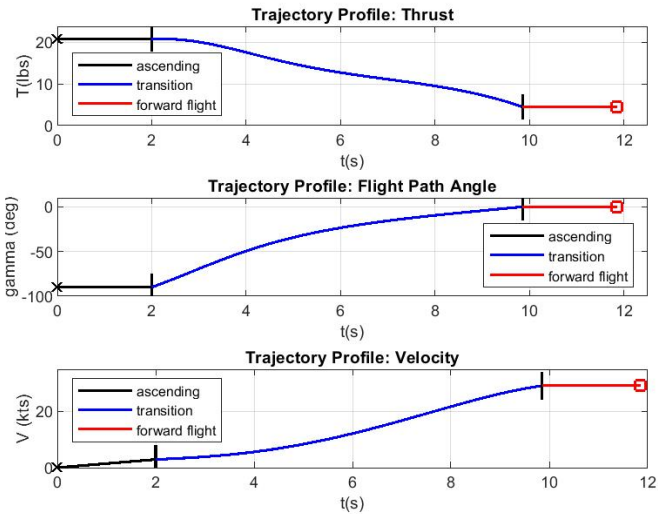

Fig. 17. Planned trajectories for command variables T, V, and γ, from hover through transition to forward flight.

Attitude/Altitude Controller

The structure of the inner-loop attitude/airspeed controller is shown in Figure 19. On receiving the estimate of the actual state $[u, v, w, \phi, \theta, \psi]^T$, $[V, \gamma, \chi, \alpha, \beta, \sigma]^T$ can be obtained via coordinate transformation. Then, the error between the actual airspeed V and the command V_{cmd} is regulated in the airspeed controller by adjusting the collective RPM ($\delta\Omega_0^{\text{fb}}$), while the commanded thrust T_{cmd} acts as the feedforward signal that provides additional collective RPM ($\delta\Omega_0^{\text{ff}}$) required for acceleration. On the other hand, in order to regulate the orientation of the airspeed and the vehicle's relative attitude towards the wind, $[\gamma_{\text{cmd}}, \chi_{\text{cmd}}, \alpha_{\text{cmd}}, \beta_{\text{cmd}}, \sigma_{\text{cmd}}]^T$ are tracked in the attitude controller by applying the differential roll RPM ($\delta\Omega_R$), pitch RPM ($\delta\Omega_P$) and yaw RPM ($\delta\Omega_Y$) respectively. Consequently, the signal $[\delta\Omega_0, \delta\Omega_R, \delta\Omega_P, \delta\Omega_Y]^T$ goes through the mixer and gets mapped to the increment of

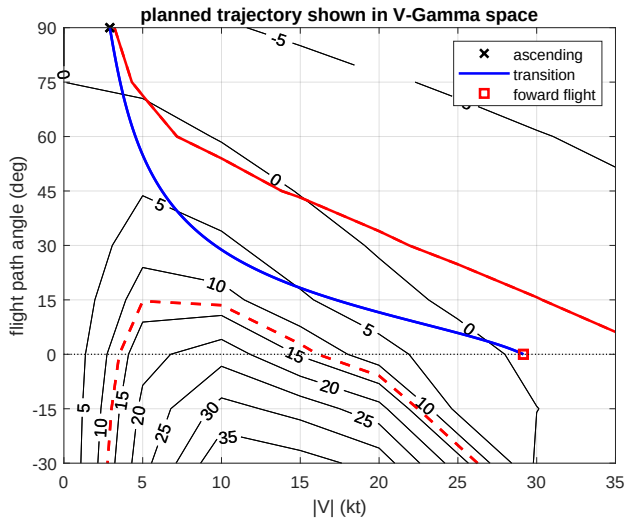

Fig. 18. Planned trajectory shown in the flight path angle versus airspeed space

the RPM for individual rotors $[\delta\Omega_1, \delta\Omega_2, \delta\Omega_3, \delta\Omega_4]^T$. By adding the increment to the trimmed RPM, the actual input $\mathbf{u} = [\Omega_1, \Omega_2, \Omega_3, \Omega_4]$ can be established.

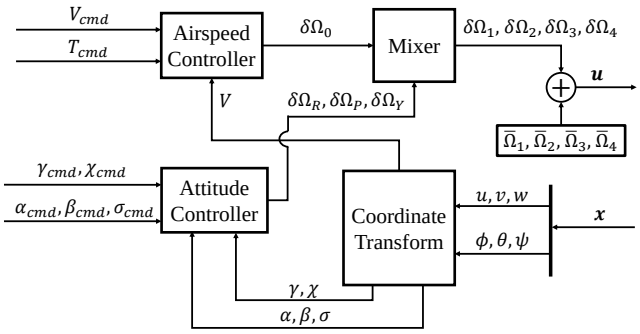

Fig. 19. Inner-loop path planner structure.

Control Methodology

We propose a *scheduled linear dynamic inversion (LDI) controller* for tracking the reference trajectory. The design of this controller requires linearization of the nonlinear dynamics at different airspeeds V and flight path angles γ, leading to the state-space model:

$$\begin{aligned} \delta\dot{\mathbf{x}} &= \mathbf{A}\delta\mathbf{x} + \mathbf{B}\delta\mathbf{u} \\ \delta\mathbf{y} &= \mathbf{C}\delta\mathbf{x} \end{aligned} \tag{15}$$

where $\delta\mathbf{x}$, $\delta\mathbf{y}$ and $\delta\mathbf{u}$ are the perturbations of state, output, and input listed in Eq.(4) and Eq.(6) *from their trimmed values*. $\mathbf{y}$ is the controlled output; the selection of the elements in $\mathbf{y}$ and the derivation of the corresponding output matrix $\mathbf{C}$ is presented in the following discussion. We note that this choice of $\mathbf{C}$ leads to $\mathbf{CB} \equiv \mathbf{0}$, and hence the second derivative of the controlled output $\mathbf{y}$ takes the form:

$$\delta\ddot{\mathbf{y}} = \mathbf{CA}^2\delta\mathbf{x} + \mathbf{CAB}\delta\mathbf{u}. \tag{16}$$

Thus, we can the choose the input to be:

$$\delta\mathbf{u} = (\mathbf{CAB})^{-1}(\delta\ddot{\mathbf{y}}_{\text{cmd}} - \mathbf{CA}^2\delta\mathbf{x}), \tag{17}$$

which simplifies the closed loop dynamics between the command $\delta\ddot{\mathbf{y}}_{\text{cmd}}$ and the actual output $\delta\mathbf{y}$ into a chain of double integrators.

In order to implement the control law in Eq.(17), $\mathbf{A}$, $\mathbf{B}$ are scheduled with respect to the current airspeed and flight path angle.

Output vector: The controlled output is selected to be:

$$\mathbf{y} = \begin{bmatrix} V & \alpha & \beta & \sigma \end{bmatrix}^T \tag{18}$$

of which all the elements can be written as functions of the elements in the state vector $\mathbf{x}$.

We can easily determine that $V = \sqrt{u^2+v^2+w^2}$. The angles α, β, and σ can be obtained analytically through the use of reference frame transformation techniques. Specifically, we use the equivalence stated before in Eq. 3:

$$T_1(\sigma)T_2(\gamma)T_3(\chi) = T_3(\beta)T_2(-\alpha)T_1(\phi)T_2(\theta)T_3(\psi)$$

Using this equation, the variables of interest (α, β, σ) can be isolated, then simplified on each side to a 3×3 matrix. Equating these elementwise, we obtain nine simultaneous equations. Solving a subset of these equations for α, β, and σ results in the following expressions (t, s and c are shorthand for tan, sin and cos functions respectively):

$$\begin{aligned} \alpha &= t^{-1}\left(\frac{c\phi s\theta c\gamma c(\psi-\chi) - c\phi c\theta s\gamma + s\phi s(\psi-\chi)s\gamma}{c\theta c(\psi-\chi)c\gamma + s\theta s\gamma}\right) \\ \beta &= s^{-1}(s\phi s\theta c(\phi-\chi)c\gamma - c\phi s(\phi-\chi)c\gamma - s\phi c\theta s\gamma) \\ \sigma &= t^{-1}\left(\frac{s\phi s\theta s\gamma c(\phi-\chi) + s\phi c\theta c\gamma - c\phi s(\phi-\chi)s\gamma}{c\phi c(\psi-\chi) + s\phi s\theta s(\psi-\chi)}\right) \end{aligned} \tag{19}$$

Thus, the analytical form of the $\mathbf{C}$ can be derived by evaluating the following matrix at the current states ϕ, ψ, θ and the prescribed $\bar{\chi}, \bar{\gamma}$:

$$\mathbf{C} = \begin{bmatrix} \frac{\partial V}{\partial u} & \frac{\partial V}{\partial v} & \cdots & \frac{\partial V}{\partial Z} \\ \frac{\partial \alpha}{\partial u} & \frac{\partial \alpha}{\partial v} & \cdots & \frac{\partial \alpha}{\partial Z} \\ \frac{\partial \beta}{\partial u} & \frac{\partial \beta}{\partial v} & \cdots & \frac{\partial \beta}{\partial Z} \\ \frac{\partial \sigma}{\partial \sigma} & \frac{\partial \sigma}{\partial v} & \cdots & \frac{\partial \sigma}{\partial Z} \end{bmatrix} \in \Re^{4\times12} \tag{20}$$

With this development, the inner loop controller design is complete.

CONCLUSION

This study examined modeling and trajectory planning of a 20 lb quadrotor biplane tailsitter through the transition maneuver from hover to forward flight. An initial model is produced

using blade element theory with 1×1 dynamic inflow and finite state interference from the rotor to the wings. A reduced order quadratic model of rotor thrust and torque coefficients is used to evaluate a momentum-theory derived wake interference model.

It is shown that lack of an interference model will produce an increase in power requirement through the transition, as the wings are guaranteed to greatly exceed stall. The importance of accurate interference modeling is shown, as depending on the model selected, the presence of the interference velocity will reduce the power requirement by up to 80%. Sufficently high interference velocities predict attachment of the flow to the wing through the entire transition maneuver.

The momentum-theory interference model is generally consistent with the finite state interference model when predicting the wing effective angle of attack at low speeds, but tends to predict a reduction in stall speed by about 2-4 kt.

The importance of accurate wing stall modeling is demonstrated for the purposes of trajectory generation. A two dimensional trim sweep through velocity magnitude and flight path angle is used to demonstrate that without interference effects, the model will always predict stalling through transition, and will overpredict the power requirement.

Finally, a trajectory planning algorithm and a linear dynamic inversion controller methodology is derived, which used a wind frame representation of the vehicle state to achieve continuous control through the transition.

Author Contact
Jean-Paul Reddinger: jean-paul.f.reddinger.civ@mail.mil
Kristoff McIntosh: mcintk3@rpi.edu
Di Zhao: zhaod3@rpi.edu
Sandipan Mishra: mishrs2@rpi.edu.

REFERENCES

[1]U.S. Army UAS Center of Excellence, Fort Rucker, AL, *U.S. Army Roadmap for Unmanned Aircraft Systems 2010-2035*, Dec. 2010.

[2]Colucci, F., "Unmanned Vertical Wingman: NGTUAS," *Vertiflite*, Vol. 67, (5), 2017, pp. 22–25.

[3]Phillips, B., Hrishikeshavan, V., Rand, O., and Chopra, I., "Design and Development of a Scaled Quadrotor Biplane with Variable Pitch Proprotors for Rapid Payload Delivery," American Helicopter Society 72nd Annual Forum, May 2016.

[4]Bogdanowicz, C., Hrishikeshavan, V., and Chopra, I., "Development of a Quad-Rotor Biplane MAV with Enhanced Roll Control Authority in Fixed Wing Mode," American Helicopter Society 71st Annual Forum, May 2015.

[5]Phillips, B., Hrishikeshavan, V., Yeo, D., and Chopra, I., "Experimental Evaluation of a Quadrotor Biplane with Variable Pitch Rotors," American Helicopter Society 73rd Annual Forum, May 2017.

[6]Phillips, B., Safieh, D., Hrishikeshavan, V., Yeo, D., and Chopra, I., "Performance and Control of Variable Pitch Proprotors for Multi-Scale Quadrotor Biplane Tailsitters (QBiTs)," Vertical Flight Society 75th Annual Forum, May. 2019.

[7]Wolfe, F., "Bell Moving to Scale Up Autonomous Delivery Drones for US Military," *Rotor & Wing International*, Sep. 27, 2017.

[8]Singh, R., Sirohi, J., and Hrishikeshavan, V., "Common Research Configuration for Collaborative Advancement of Scalable VTOL UAS Technologies," Vertical Flight Society 75th Annual Forum, May. 2019.

[9]Reddinger, J., "Performance and Controls of a Scalable Quadrotor Biplane Tailsitter," AIAA Scitech 2019 Forum, Jan. 2019.
doi: 10.2514/6.2019-1287

[10]Nogar, S. M. and Kroninger, C. M., "Development of a Hybrid Micro Air Vehicle Capable of Controlled Transition," *IEEE Robotics and Automation Letters*, Vol. 3, (3), Jul. 2018, pp. 2269–2276.
doi: 10.1109/LRA.2018.2800797

[11]Misiorowski, M., Gandhi, F., and Anusonti-Inthra, P., "Computational Analysis of Rotor-Blown-Wing for E-VTOL Applications," Vertical Flight Society 75th Annual Forum, May. 2019.

[12]Ryseck, P., Yeo, D., Hrishikeshavan, V., and Chopra, I., "Aerodynamic and Mechanical Design of a Morphing Winglet for a Quadrotor Biplane Tail-sitter," 8th Autonomous VTOL Technical meeting & 6th Electric VTOL Symposium, Jan. 2019.

[13]Russell, C., Willink, G., Theodore, C., Jung, J., and Glasner, B., "Wind Tunnel and Hover Performance Test Results for Multicopter UAS Vehicles," Technical report, NASA/TM–2018–219758, Feb. 2018.